ACS APPLIED MATERIALS & INTERFACES

Research Article

www.acsami.org

Anodic WO_3 Mesosponge @ Carbon: A Novel Binder-less Electrode for Advanced Energy Storage Devices

Syed Atif Pervez,[†,‡] Doohun Kim,*[,†] Chil-Hoon Doh,[†,‡] Umer Farooq,[†,‡] Hae-Young Choi,[†] and Jung-Hee Choi[†]

[†]Korea Electro-technology Research Institute (KERI), Changwon 642-120, Republic of Korea

[‡]Electrical Functionality Material Engineering (KERI Campus), Korea University of Science and Technology, Daejeon 305-333, Republic of Korea

Supporting Information

ABSTRACT: A novel design for an anodic WO_3 mesosponge @ carbon has been introduced as a highly stable and long cyclic life Li-ion battery electrode. The nanocomposite was successfully synthesized via single-step electrochemical anodization and subsequent heat treatment in an acetylene and argon gas environment. Morphological and compositional characterization of the resultant materials revealed that the composite consisted of a three-dimensional interconnected network of WO_3 mesosponge layers conformally coated with a 5 nm thick carbon layer and grown directly on top of tungsten metal. The results demonstrated that the carbon-coated mesosponge WO_3 layers exhibit a capacity retention of 87% after completion of 100 charge/discharge cycles, which is significantly higher than the values of 25% for the crystalline (without carbon coating) or 40% for the as-prepared mesosponge WO_3 layers. The improved electrochemical response was attributed to the higher stability and enhanced electrical conductivity offered by the carbon coating layer.

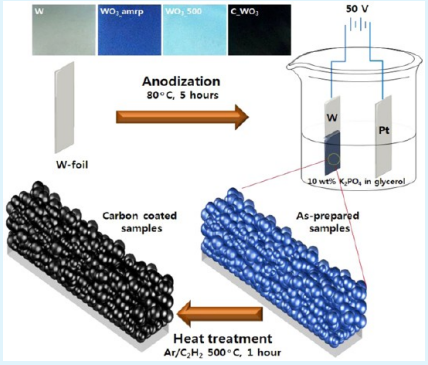

KEYWORDS: *mesosponge, WO_3, carbon-coating, anodization, battery*

INTRODUCTION

In recent years, Li-ion batteries (LIBs) have attracted considerable scientific interest for their great potential in consumer electronic devices, electric vehicles, and military and aerospace applications.[1−5] The market expansion of LIBs has resulted in increased demand with improved energy and power density and long cyclic life while maintaining low production costs. Transition metal oxides (TMOs) are considered to be suitable alternative anode materials to fulfill these demands due to their higher specific capacity than that of commercial graphite, widespread availability, and better safety features.[6−9] The higher capacity delivered by TMOs is due to their novel conversion reaction with lithium.[10] However, most TMOs suffer from large volume expansion/contraction upon lithium insertion/deinsertion, resulting in material degradation and, hence, poor cyclic performance. To address this issue, nanostructuring of the material is an efficient strategy. With proper design and engineering, the nanostructured electrode material can offer enough void space to accommodate the volumetric expansion, consequently improving the cyclic performance.[9,11,12] Another widely adopted approach for enhancing the stability of the electrode material is coating, surface modification, or encapsulation of the active material with carbon.[13−17] Carbon, owing to its stability and higher conductivity, limits the volume expansion of the electrode during lithiation/delithiation and offers improved electron conduction during battery performance.

As an anode material for LIB, tungsten oxide has recently attracted attention due to its abundant availability, environmental benignity, low cost, better safety, and higher theoretical capacity (693 mAh/g) compared to commercial graphite anode.[18−24] Such a high theoretical capacity is achieved due to the lithium conversion reaction, which requires the formation of tungsten metal and lithium oxide, as given below:

$$WO_3 + 6Li^+ + 6e^- \rightarrow W + 3Li_2O$$

However, as with other metal oxides, tungsten oxide also experiences significant volume changes during lithiation/delithiation, resulting in severe degradation in its cyclic performance. To address this issue, researchers have performed nanostructuring of the material the form of nanospheres,[18,19] nanorods,[21,22] nanowires,[23] and mesosporous structures.[24] Additionally, attention has been given to synthesizing carbon/metal-oxide nanocomposites to take advantage of carbon to improve the stability of the electrode material. However, most of these synthesis techniques require complex procedures and high cost, such as high pressure and temperature using

Received: January 13, 2015
Accepted: March 20, 2015
Published: March 20, 2015

DOI: 10.1021/acsami.5b00341
ACS Appl. Mater. Interfaces 2015, 7, 7635−7643

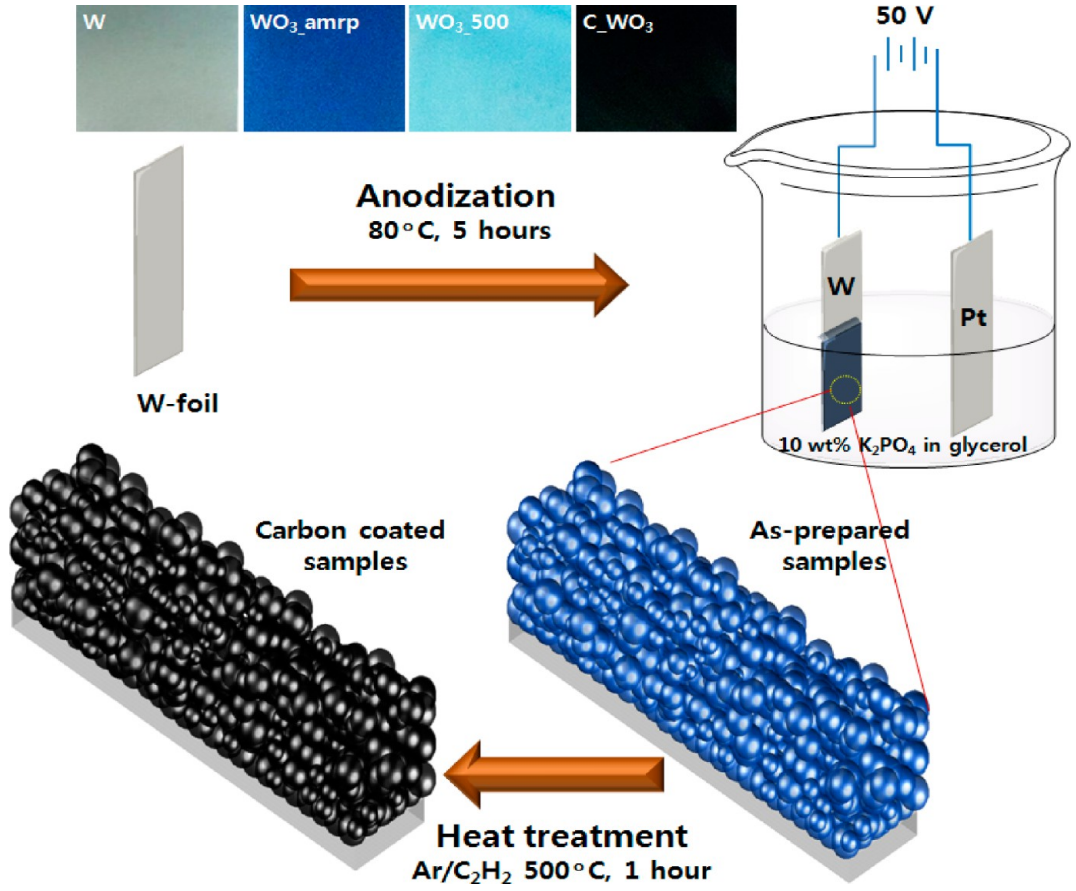

Figure 1. Schematic diagram of the synthesis process for mesosponge C_WO_3 layers.

autoclaves,[17,21−23] pyrolysis using expensive and complicated experiment setups,[19] or template replication involving multiple steps and high resource consumption.[24] Furthermore, most of the reported works follow the conventional method of electrode preparation, in which a certain weight percentage of the active material, polymeric binder and carbon additives are mixed and casted on current collectors. This technique has a major disadvantage in that 70−80% of the active material weight is utilized, while the remaining 30−20% acts as "dead weight" added to the electrode. Therefore, more recent research has focused on the fabrication of electrode material without binder and conductive additives, hence fully utilizing the active materials.[25−28]

Melody et al.[29] reported for the first time on the growth of valve metals in electrolytes containing glycerol and dipotassium phosphate dibasic at high temperatures in the range of 150−180 °C. The same approach was then extended by the Schmuki group[30−32] to synthesize a mesosponge of transition metals such as Ti and W. Herein, we have synthesized anodic WO_3 mesosponge layers and demonstrated their feasibility as binder-less and conductive additive-free electrodes for LIBs. Furthermore, to limit the volume expansion during lithiation/delithiation, we have heat-treated the as-prepared samples in an acetylene and argon gas (C_2H_2/Ar) environment to obtain a conformal carbon coating. The results show improved capacity retention for the carbon-coated samples (C_WO_3) in comparison to either as-prepared (WO_3_amrp) or crystalline samples (WO_3_500, WO_3_300).

EXPERIMENTAL SECTION

Material Synthesis. All the reagents were of analytical grade and used without further purification. WO_3 mesosponge layers were grown by electrochemical anodization conducted by applying 50 V for 5 h between a degreased tungsten (W) foil (0.1 mm thickness, 99.99% purity, Nilaco Japan) as anode and platinum mesh as cathode in an electrolyte maintained at a temperature of 80 °C. The anodization current was recorded via computer with Labview software (Agilent). Prior to anodization, the electrolyte was heated at 180 °C for 3 h to evaporate the water content from the solution. The electrolyte solution was a mixture of 10 wt % potassium phosphate dibasic in glycerol.[31] After anodization, the samples were initially stored overnight in ethanol, then rinsed, and finally dried in an oven. The heat treatment of the as-prepared samples was performed in a furnace (XY-1400S, Hantech, Korea) at 500 °C for 1 h either under C_2H_2/Ar or ambient air environment.

Material Characterization. The morphology of the mesosponge layers was determined via field-emission scanning electron microscopy (FE-SEM; Hitachi S4800). The transmission electron microscopy (TEM) images and selected area electron diffraction (SAED) patterns were obtained via TEM (Philips TF30ST). To prepare the TEM samples, the oxide layer was scratched from the W foil surface and dispersed onto a carbon grid. The crystalline phase of the synthesized material was confirmed via X-ray diffraction (XRD) analysis using an X-ray diffractometer (Philips X'pert-MPD) with a Panalytical X'celerator detector with graphite monochromized Cu Kα radiation (λ = 1.54056 Å). Rietveld analysis was conducted for the XRD spectra using the GSAS package.[33] The Raman spectra were obtained using a Raman spectrometer (NTEGRA SPECTRA NT, MDT) with a laser excitation wavelength of 532 nm.

Electrochemical Measurements. Coin half cells were assembled in a dry room to evaluate the electrochemical performance of the material. WO_3 mesosponge layers grown on top of the W current

DOI: 10.1021/acsami.5b00341
ACS Appl. Mater. Interfaces 2015, 7, 7635−7643

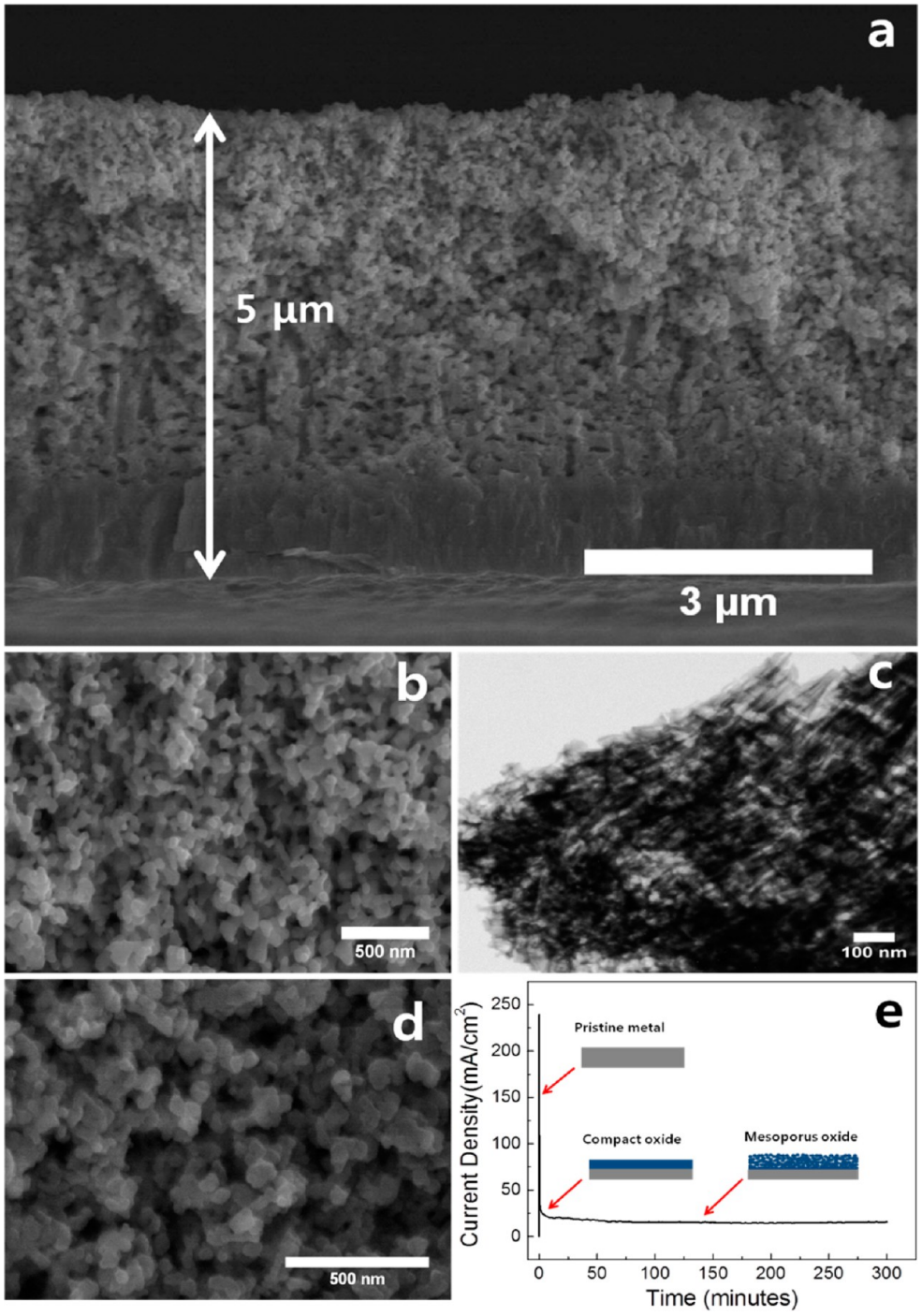

Figure 2. Mesosponge C_WO_3 layers (a and b) cross-sectional FE-SEM images, (c) TEM image, and (d) top view image and (e) current−time transient curve for the anodization process.

collector served as the working electrode with a polypropylene membrane (Celgard 2325, Celgard, Inc., Charlotte, NC) as a separator and Li-metal (purity 99.9%) as the counter electrode. The electrolyte was 1.2 M $LiPF_6$ in ethylene carbonate/dimethyl carbonate (1:1, v/v). The assembled cells had an open circuit voltage of approximately 3 V and were galvanostatically charged/discharged at current densities ranging from 100 to 1500 $\mu A/cm^2$ across a potential range of 0.005−3 V using a multichannel battery tester (TOYO TOSCAT-3100U). Cyclic voltammetry (CV) and electrochemical impedance spectroscopy (EIS) were conducted via an electrochemical setup (model VMP3, Bio Logic, France). CV was performed at a 0.1 mV/s scan rate in a voltage range of 0.005−3 V, while EIS was performed at different bias potentials in a frequency range of 10 kHz to 100 MHz with an AC signal amplitude of 10 mV.

RESULTS AND DISCUSSION

Figure 1 shows the schematic representation of the synthesis process for C_WO_3 layers. Following the electrochemical anodization step, the as-prepared samples were further heat treated in a C_2H_2/Ar environment to obtain carbon coated samples. Both the carbon-coated and the as-prepared samples were 3D mesosponge layers of WO_3 grown on top of W foil with and without carbon layer, respectively. By the naked eye,

DOI: 10.1021/acsami.5b00341
ACS Appl. Mater. Interfaces 2015, 7, 7635−7643

change in the sample color was observed for each step of the synthesis, as shown in Figure 1 and Figure S1 (Supporting Information).

Figure 2a–d shows the FE-SEM and TEM images of the C_WO_3 sample. A series of anodization experiments were conducted to obtain a suitable thickness for the mesosponge oxide layer by varying the anodization time at a constant temperature and voltage, as shown in Figure S2 (Supporting Information). The optimized anodization conditions were 50 V for 5 h at 80 °C, which yielded a thickness of approximately 5 μm, as shown in Figure 2a. For carbon coating, the samples were heat treated in a tube furnace under a C_2H_2/Ar environment with a ratio of 2:10 at 500 °C for 1 h. The morphology of the mesosponge layers remained essentially the same before and after carbon coating. Closer inspection of the cross-sectional images revealed that the anodized layer consists of nanoparticles with an average dimension of 60 nm, interconnected in a continuous three-dimensional (3D) architecture with a uniform layer thickness (Figure 2b,c and Figure S3, Supporting Information). In addition, these layers are strongly adhered to the W-metal surface, which acts as a current collector (Figure S4, Supporting Information). From the top view of the C_WO_3 layer image shown in Figure 2d, another set of pores is found to be uniformly distributed along the surface with an average feature size of 50 nm (Figure S3, Supporting Information). This 3D structure with interconnected pores allows a large surface area for lithium storage while providing enough void space to accommodate volumetric expansion during lithiation/delithiation. In Figure 2e, a current–time transient curve for the anodization procedure is shown. Anodization of metal oxides is normally governed by such a curve, which gives information about different stages of the growth of the oxide layers.[34] From the figure, it is evident that upon voltage application, a high current value sets in due to the enhanced conductivity offered by the pristine W foil. However, an abrupt fall in the current is soon observed due to the formation of a compact oxide layer on the metal surface. Finally, the current levels off, which indicates a balance between the formation and etching of the oxide layer and hence a regular mesosponge layer formation.

Figure 3 shows the XRD and Raman analysis for the mesosponge WO_3 layers. For WO_3_500, the XRD patterns were refined through Reitveld calculations, as shown in Figure 3a, to quantify the phase and crystal structure of the material. The observed reflections suggest the formation of a monoclinic structure of WO_3. The calculated lattice parameters are found to be a = 7.339 Å, b = 7.592 Å, and c = 7.714 Å with a unit cell volume of 429.838 Å^3, which are consistent with the literature values (JCPDS No. 43-1035) and indexed according to the $P121/n1$ space group. Figure 3b shows the XRD comparison of WO_3 mesosponge layers before and after heat treatment in air and in a C_2H_2/Ar environment. For WO_3_amrp, prior to the heat treatment no diffraction peaks are observed suggesting an amorphous structure. The only peak observed in the pattern is due to the W substrate. When the samples are annealed at 300 and 500 °C, the material changes from amorphous to monoclinic crystalline phase of WO_3, which is in agreement with the Reitveld analysis. It is observed that increasing the temperature from 300 to 500 °C results in the sharpening of the diffraction peaks, suggesting improvement in the crystallinity of the material with increased temperature. For the C_WO_3 samples, the presence of the monoclinic phase is also confirmed, albeit with a slight decrease in the intensities of the

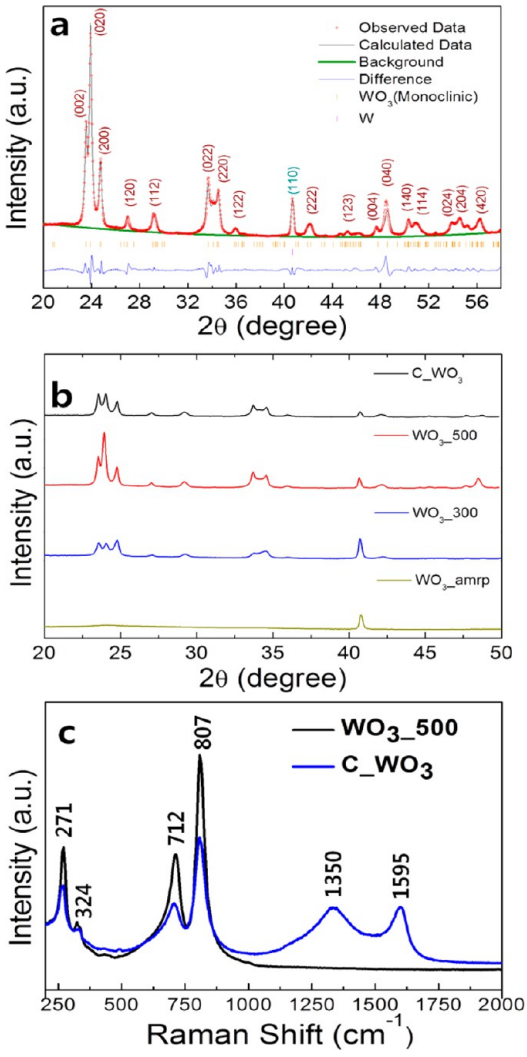

Figure 3. (a) Reitveld refined XRD patterns for WO_3_500 [Monoclinic (JCPDS no. 43-1035)]; (b) XRD comparison of WO_3 mesosponge layers before and after heat treatment in air and C_2H_2/Ar environment; (c) Raman spectra for mesosponge WO_3 layers both with and without carbon coating.

diffraction peaks mainly due to the amorphous carbon coated on the structure.[17,27] It is worth mentioning here that because the carbon layer is amorphous, no additional peaks for carbon are observed in the patterns. Furthermore, the presence of all the characteristic peaks corresponding to the monoclinic phase of WO_3 indicates no change in the crystallinity of the material after carbon coating. The Raman spectra in Figure 3c further confirms the crystallinity of the material and the presence of carbon in the structure. For both samples WO_3_500 and C_WO_3, the strong bands at 712 and 807 cm^{-1} are attributed to the ν(O–W–O) stretching modes, while the weaker bands at 271 and 324 cm^{-1} are assigned to the δ(O–W–O) bending modes of the monoclinic WO_3.[35] Comparing the two spectra clearly suggests a decrease in the intensity of the Raman peaks for C_WO_3, which agrees well with the XRD study. Furthermore, the presence of D and G bands at 1350 and 1595 cm^{-1} confirms the presence of carbon in the structure.

TEM analysis of both the as-prepared and carbon-coated samples is presented in Figure 4. In contrast to WO_3_amrp, the C_WO_3 samples clearly show a conformal coating of WO_3 with an amorphous carbon layer with a thickness of approximately 5

DOI: 10.1021/acsami.5b00341
ACS Appl. Mater. Interfaces 2015, 7, 7635–7643

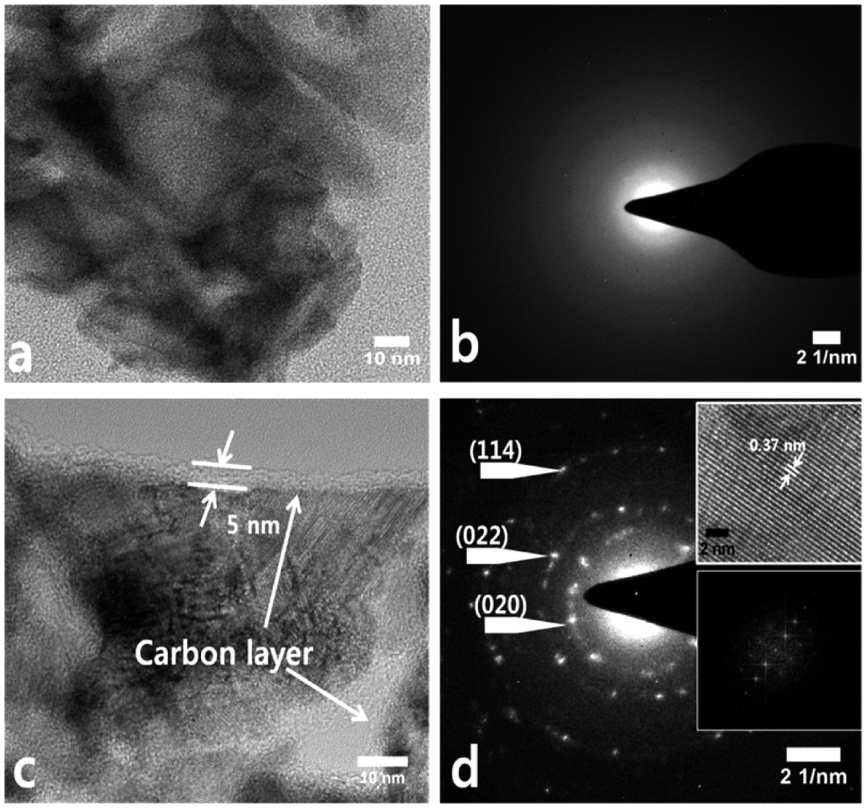

Figure 4. (a and b) TEM images and SAED pattern for WO_3_amrp; (c and d) TEM images and SAED pattern for C_WO_3. (d, insets) HRTEM with corresponding FFT of the C_WO_3.

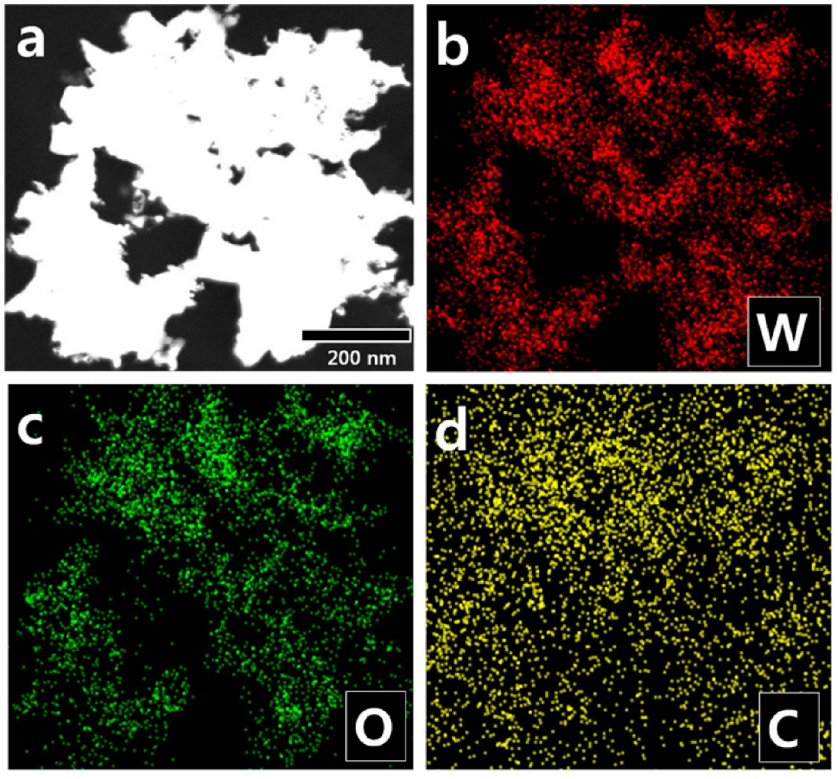

Figure 5. (a) Dark field TEM image for mesosponge C_WO_3 and TEM elemental mapping for (b) W, (c) O, and (d) C in the structure.

nm (Figure 4a,c). The presence of this layer is crucial to the enhanced electrochemical performance of the C_WO_3 based anode. From the SAED analysis for WO_3_amrp in Figure 4b, the absence of diffraction rings clearly demonstrates the amorphous nature of the material. In contrast, the bright diffraction rings in the SAED pattern for C_WO_3 suggest the

DOI: 10.1021/acsami.5b00341
ACS Appl. Mater. Interfaces 2015, 7, 7635−7643

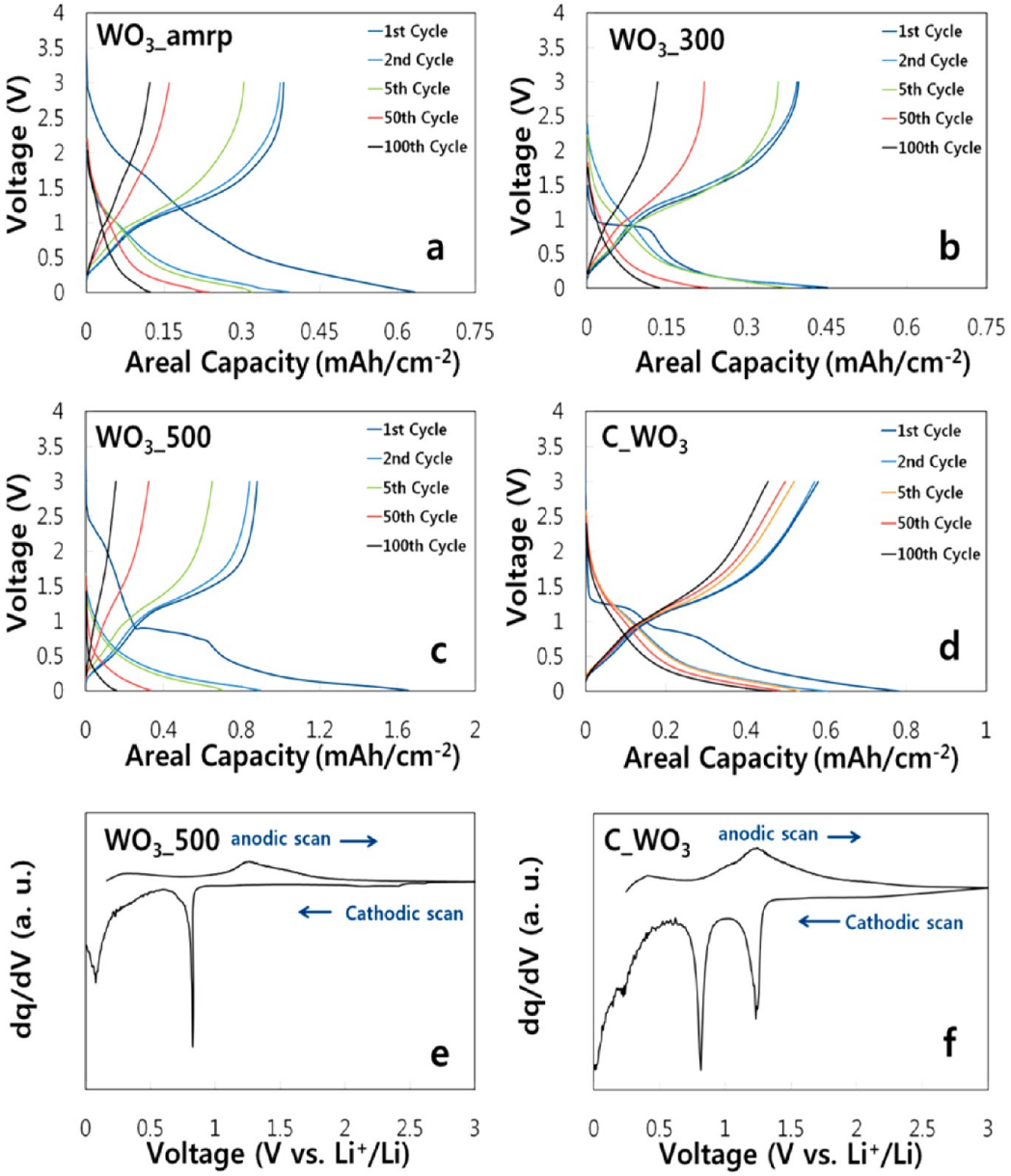

Figure 6. Selected galvanostatic charge/discharge curves obtained at a current density of 100 μA/cm^2 between 0.005 and 3 V for (a) WO_3_amrp, (b) WO_3_300, (c) WO_3_500, and (d) C_WO_3. First cycle dq/dV plots for (e) WO_3_500 and (f) C_WO_3.

polycrystalline nature of the material (Figure 4d). The indexing of the SAED rings pattern is identical to the [020], [022] and [114] planes of the monoclinic phase of WO_3 (JCPDS No. 43-1035), as in the XRD spectra discussed earlier. The HRTEM image further provides structural insight on the material (Figure 4d, inset). The *d*-spacing of the lattice fringes of WO_3 crystallites is found to be 0.37 nm, which corresponds to the [020] plane of the monoclinic WO_3 crystal lattice. Moreover, the fast Fourier transform analysis of C_WO_3 further highlights the improved crystallinity of the material (Figure 4d, inset). In Figure 5, the TEM elemental mapping of C_WO_3 is presented to provide insight into the presence and distribution of carbon atoms in the structure. As shown, a homogeneous spatial distribution of carbon over the entire volume of the mesosponge structure is observed. This analysis was also supported by the energy dispersive X-ray spectrum (Figure S5, Supporting Information), where the results are tabulated in terms of weight and atomic percentages. Alongside W and O, an atomic percentage of 52.8 is confirmed for C.

To evaluate the electrochemical response in terms of the lithium insertion/deinsertion, we cycled the material for 100 consecutive cycles. For clarity, only the 1st, 2nd, 5th, 50th, and 100th charge/discharge cycles for all samples are shown in Figure 6. The electrode was cycled at 100 μA/cm^2 for the first four cycles to obtain a stable solid electrolyte interface (SEI) layer formation[36] and then at 200 μA/cm^2 for the remaining 96 cycles in a voltage range of 0.005−3.0 V. The open circuit voltage for each cell was approximately 3 V (vs Li^+). The areal capacity was calculated by considering the active surface area of 1 cm^2 of the anodized WO_3 layer. Considering the first discharge cycle for each sample, it is evident from the figure that all the samples heat treated either in air (WO_3_300, WO_3_500) or in a C_2H_2/Ar environment (C_WO_3) exhibit characteristic voltage plateaus, unlike the non-heat-treated sample (WO_3_amrp). The voltage plateaus for the crystalline

DOI: 10.1021/acsami.5b00341
ACS Appl. Mater. Interfaces 2015, 7, 7635−7643

samples are indicative of the lithium insertion/extraction from their monoclinic crystal structure. WO_3_amrp, however, lacks a proper crystal structure, with random locations for lithium insertion, and hence a sloping discharge curve without any prominent plateau is observed.[25,26,37] For the crystalline samples, C_WO_3 shows two voltage plateaus at ca. 1.2 V and ca. 0.8 V, while WO_3_300 and WO_3_500 show a single voltage plateau at ca. 0.8 V. The two voltage plateaus in C_WO_3 are indicative of a coexistence of Li intercalation in the structure and the reduction of W ions to form nanometer W metal and amorphous Li_2O,[26] as given below:

$$WO_3 + xLi^+ + xe^- \rightarrow Li_xWO_3$$

$$Li_xWO_3 + (6 - x)Li^+ + (6 - x)e^- \rightarrow W + 3Li_2O$$

Similarly, for the first charge cycle, a voltage plateau at ca. 1.2 V is observed for all the crystalline samples. These voltage plateaus are clearly reflected during the respective cathodic and anodic scans for WO_3_500 and C_WO_3 in the differential capacity vs voltage plots obtained for the first charge/discharge cycle (Figure 6e,f). For WO_3_500, the cathodic/anodic scan peaks occur at 0.8/1.2 V, while for C_WO_3 they occur at 1.2,0.8/1.2 V. The amorphous sample, as expected, does not show any distinct peak in the cathodic scan (Figure S6, Supporting Information), indicating the lack of crystallinity of the material.

Table 1 shows the charge capacities for WO_3_amrp, WO_3_300, WO_3_500, and C_WO_3 during the 1st, 2nd, 5th, 50th, and 100th cycles at 100 and 200 $\mu A/cm^2$ and their percentage capacity degradation (% C_d) after the completion of 100 cycles. The analysis clearly shows that the % C_d in the samples without carbon coating is quite severe. For example, in the case of WO_3_500, a C_d of 75% is recorded from the 5th to the 100th cycle, which is significantly higher than the value of 13% for C_WO_3. This stable cyclic performance for C_WO_3 clearly demonstrates the effectiveness of carbon coating in suppressing the volumetric expansion during lithiation/delithiation and, hence, improving the overall electrochemical performance.

Table 1. Charge Capacity Values for Selected Cycles for WO_3_amrp, WO_3_300, WO_3_500, and C_WO_3 and Their Respective Percent Capacity Degradation after Completion of the 100th Cycle

	charge capacity (mAh/cm^2)					
	@ 100 $\mu A/cm^2$		@ 200 $\mu A/cm^2$			
sample	1st	2nd	5th	50th	100th	% C_d
WO_3_amrp	0.38	0.37	0.30	0.16	0.12	60
WO_3_300	0.40	0.39	0.35	0.22	0.13	63
WO_3_500	0.88	0.84	0.65	0.32	0.16	75
C_WO_3	0.57	0.57	0.52	0.50	0.45	13

Figure 7a shows a comparison of the cyclic performance in terms of capacity retention for all samples. The figure reveals an initial areal capacity of ca. 0.38, 0.40, and 0.88 mAh/cm^2 for WO_3_amrp, WO_3_300, and WO_3_500, respectively, demonstrating a gradual increase in the capacity upon increased heat treatment. This increase in capacity may be attributed to the improvement in the crystallinity of the material from an amorphous to a monoclinic WO_3 structure. The crystalline WO_3 offers a three-dimensional framework offering short, multidirectional transport lengths, which favor rapid lithium ion diffusivity and electron transport.[25] It is, however, observed that a significant degradation in the capacity occurs for all these samples upon extended cycling due to the aggregation and pulverization of the particles caused by the large volume change during cycling (quantitative data: Table 1). C_WO_3, in contrast, shows a stable cycling performance, as after the completion of 100 cycles, only 13% of the initial capacity (5th cycle) is lost. This improved performance is attributed to the presence of a carbon layer in the structure, which provides sufficient buffer against the volumetric change in the material upon lithium insertion/deinsertion.

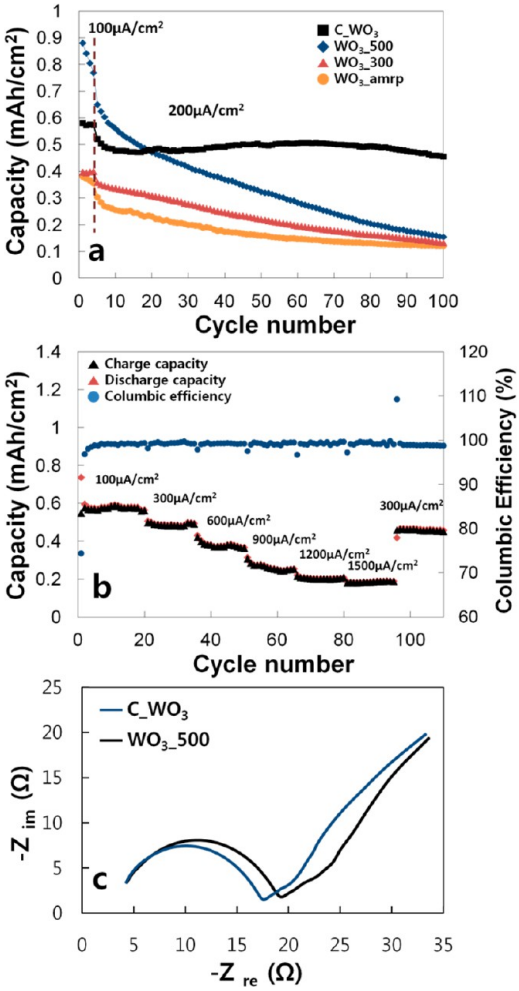

Figure 7. (a) Cyclic performance test for WO_3_amrp, WO_3_300, WO_3_500, and C_WO_3. (b) Rate capability tests and Coulombic efficiency for C_WO_3 evaluated at various current densities from 100 to 1500 μAcm^{-2}. (c) Comparative electrochemical impedance spectra of C_WO_3 and WO_3_500 in the form of Nyquist plots obtained after the completion of 10 cycles.

For high-performance LIBs, the device response at high current rates is crucial; therefore, a rate capability test of the electrode materials was conducted. For the test, the C_WO_3 electrode was cycled at different current densities ranging from 100 to 1500 $\mu A/cm^2$ and then back to the initial moderate current density of 300 $\mu A/cm^2$. As shown in Figure 7b, the reversible areal capacities of electrode cycling at progressively increasing current densities are ca. 0.57, 0.50, 0.40, 0.27, 0.20, and 0.19 mAh/cm^2, respectively. When the current density switches back from 1500 to 300 $\mu A/cm^2$, the reversible capacity

DOI: 10.1021/acsami.5b00341
ACS Appl. Mater. Interfaces 2015, 7, 7635−7643

recovers to ca. 0.45 mAh/cm^2, indicating swift response of the electrode and a good capacity recovery. It is also observed that even at higher current densities and after prolonged cycling, the charge/discharge profiles exhibit similar characteristic voltage plateaus, indicating excellent stability of the material (Figure S7, Supporting Information). Furthermore, high Coulombic efficiency of ca. 99% for all the cycles at different current densities indicates an excellent reversibility of the material during cycling. It is important to mention here that the relatively low Coulombic efficiency during the first few cycles is quite common in nanostructured electrodes.[36,38] The lower Coulombic efficiency indicates higher irreversible capacity because of the excess high capacity during the first discharge cycle, attributed to the formation of the SEI layer and possible interfacial lithium storage.

EIS was conducted at room temperature to gain further insight into the electrochemical performance of the synthesized samples. Figure 7c shows a comparison of the EIS spectra for C_WO_3 and WO_3_500, obtained after completion of 10 cycles. Both spectra are similar in shape, with a semicircle in the high-medium frequency range and a sloping line in the low frequency range. The semicircle indicates the charge transfer resistance of the electrode, while the sloping line is attributed to Warburg impedance, providing information about the lithium ion diffusion inside the structure.[39] From the figure, it is evident that the diameter of the semicircle is smaller in the case of C_WO_3 than in WO_3_500. This result indicates that the presence of carbon assists in improved charge transfer kinetics and, hence, overall enhanced electrochemical performance.

CONCLUSIONS

In summary, mesosponge tungsten oxide layers grown via electrochemical anodization were demonstrated as a potential candidate for LIB anodes. The electrode design was binder-less and free of conductive additives. The as-prepared samples consisted of a 3D network of nanosized WO_3 particles interconnected in an ordered fashion and conformally coated by carbon layers a few nanometers thick. A comprehensive morphological and compositional characterization was performed for all samples to confirm their crystallinity and the presence of carbon. The results showed a superior electrochemical performance for C_WO_3 over the rest of the samples in terms of capacity retention. The rate performance and Coulombic efficiency of the C_WO_3 were also quite remarkable. The improved electrochemical performance was attributed to the 3D architecture of the anodized mesosponge morphology and the higher electrical conductivity/stability of the carbon layer.

ASSOCIATED CONTENT

Supporting Information

Additional SEM images, EDS spectra with their quantitative results, particle size analysis, CV plots, charge/discharge curves, and digital images of the samples at different synthesis stages. This material is available free of charge via the Internet at http://pubs.acs.org.

AUTHOR INFORMATION

Corresponding Author

*E-mail: kdh0121@keri.re.kr.

Notes

The authors declare no competing financial interest.

ACKNOWLEDGMENTS

This study was supported by the Korea Research Council for Industrial Science & Technology (ISTK, KERI_15-12-N0101-57).

REFERENCES

(1) Idota, Y.; Kubota, T.; Matsufuji, A.; Maekawa, Y.; Miyasaka, T. Tin-based Amorphous Oxide: A High-Capacity Lithium-Ion-Storage Material. *Science* **1997**, *276*, 1395−1397.

(2) Poizot, P.; Laruelle, S.; Grugeon, S.; Dupont, L.; Tarascon, J.-M. Nano-Sized Transition-Metal Oxides as Negative-Electrode Materials for Lithium-Ion Batteries. *Nature* **2000**, *407*, 496−499.

(3) Croce, F.; Appetecchi, G. B.; Persi, L.; Scrosati, B. Nanocomposite Polymer Electrolytes for Lithium Batteries. *Nature* **1998**, *394*, 456−458.

(4) Amine, K.; Liu, J.; Belharouak, I. High-Temperature Storage and Cycling of C-LiFePO$_4$/Graphite Li-Ion Cells. *Electrochem. Commun.* **2005**, *7*, 669−673.

(5) Peled, E.; Menachem, C.; Bar-Tow, D.; Melman, A. Improved Graphite Anode for Lithium-Ion Batteries Chemically: Bonded Solid Electrolyte Interface and Nanochannel Formation. *J. Electrochem. Soc.* **1996**, *143*, L4−L7.

(6) Ortiz, G. F.; Hanzu, I.; Knauth, P.; Lavela, P.; Tirado, J. L.; Djenizian, T. TiO$_2$ Nanotubes Manufactured by Anodization of Ti Thin Films for On-Chip Li-Ion 2D Microbatteries. *Electrochim. Acta* **2009**, *54*, 4262−4268.

(7) Wang, Y.; Zhang, H. J.; Lu, L.; Stubbs, L. P.; Wong, C. C.; Lin, J. Designed Functional Systems from Peapod-like Co@Carbon to Co$_3$O$_4$@Carbon Nanocomposites. *ACS Nano* **2010**, *4*, 4753−4761.

(8) Zhu, X.; Zhu, Y.; Murali, S.; Stoller, M. D.; Ruoff, R. S. Nanostructured Reduced Graphene Oxide/Fe$_2$O$_3$ Composite as a High-Performance Anode Material for Lithium Ion Batteries. *ACS Nano* **2011**, *5*, 3333−3338.

(9) Pervez, S. A.; Kim, D.; Farooq, U.; Yaqub, A.; Choi, J.-H.; Lee, Y.-J.; Doh, C.-H. Comparative Electrochemical Analysis of Crystalline and Amorphous Anodized Iron Oxide Nanotube Layers as Negative Electrode for LIB. *ACS Appl. Mater. Interfaces* **2014**, *6*, 11219−11224.

(10) Cabana, J.; Monconduit, L.; Larcher, D.; Palacín, M. R. Beyond Intercalation-Based Li-Ion Batteries: The State of the Art and Challenges of Electrode Materials Reacting Through Conversion Reactions. *Adv. Mater.* **2010**, *22*, E170−E192.

(11) Wu, H. B.; Chen, J. S.; Hng, H. H.; Wen Lou, X. Nanostructured Metal Oxide-Based Materials as Advanced Anodes for Lithium-Ion Batteries. *Nanoscale* **2012**, *4*, 2526−2542.

(12) Bruce, P. G.; Scrosati, B.; Tarascon, J.-M. Nanomaterials for Rechargeable Lithium Batteries. *Angew. Chem., Int. Ed.* **2008**, *47*, 2930−2946.

(13) Xia, H.; Wan, Y.; Yuan, G.; Fu, Y.; Wang, X. Fe$_3$O$_4$/Carbon Core−Shell Nanotubes as Promising Anode Materials for Lithium-Ion Batteries. *J. Power Sources* **2013**, *241*, 486−493.

(14) Wang, B.; Wang, G.; Zheng, Z.; Wang, H.; Bai, J.; Bai, J. Carbon Coated Fe$_3$O$_4$ Hybrid Material Prepared by Chemical Vapor Deposition for High Performance Lithium-Ion Batteries. *Electrochim. Acta* **2013**, *106*, 235−243.

(15) Kang, K.-Y.; Lee, Y.-G.; Kim, S.; Seo, S. R.; Kim, J.-C.; Kim, K. M. Electrochemical Properties of Carbon-Coated TiO$_2$ Nanotubes as a Lithium Battery Anode Material. *Mater. Chem. Phys.* **2012**, *137*, 169−176.

(16) Zhang, J.; Yan, X.; Zhang, J.; Cai, W.; Wu, Z.; Zhang, Z. Preparation and Electrochemical Performance of TiO$_2$/C Composite Nanotubes as Anode Materials of Lithium-Ion Batteries. *J. Power Sources* **2012**, *198*, 223−228.

(17) Yoon, S.; Woo, S.-G.; Jung, K.-N.; Song, H. Conductive Surface Modification of Cauliflower-like WO_3 and Its Electrochemical Properties for Lithium-Ion Batteries. *J. Alloys Compd.* **2014**, *613*, 187−192.

DOI: 10.1021/acsami.5b00341
ACS Appl. Mater. Interfaces 2015, 7, 7635−7643

(18) Sasidharan, M.; Gunawardhana, N.; Yoshio, M.; Nakashima, K. WO_3 Hollow Nanospheres for High-Lithium Storage Capacity and Good Cyclability. *Nano Energy* **2012**, *1*, 503−508.
(19) Sim, C. M.; Hong, Y. J.; Kang, Y. C. Electrochemical Properties of Yolk-Shell, Hollow, and Dense WO_3 Particles Prepared by using Spray Pyrolysis. *ChemSusChem* **2013**, *6*, 1320−1325.
(20) Huang, K.; Zhang, Q. Rechargeable Lithium Battery Based on a Single Hexagonal Tungsten Trioxide Nanowire. *Nano Energy* **2012**, *1*, 172−175.
(21) Kai, H.; Qingtao, P.; Feng, Y.; Shibing, N.; Xiucheng, W.; Deyan, H. Controllable Synthesis of Hexagonal WO_3 Nanostructures and their Application in Lithium Batteries. *J. Phys. D: Appl. Phys.* **2008**, *41*, 155417−155422.
(22) Xin-Yu, X.; Bin, H.; Shuang, Y.; Li-Li, X.; Zhao-Hui, C.; Chun-hua, M. SnO_2/WO_3 Core−Shell Nanorods and their High Reversible Capacity as Lithium-Ion Battery Anodes. *Nanotechnology* **2011**, *22*, 395702−395707.
(23) Yu, M.; Sun, H.; Sun, X.; Lu, F.; Hu, T.; Wang, G.; Qiu, H.; Lian, J. 3D WO_3 Nanowires/Graphene Nanocomposite with Improved Reversible Capacity and Cyclic Stability for Lithium Ion Batteries. *Mater. Lett.* **2013**, *108*, 29−32.
(24) Yoon, S.; Jo, C.; Noh, S. Y.; Lee, C. W.; Song, J. H.; Lee, J. Development of a High-Performance Anode for Lithium Ion Batteries using Novel Ordered Mesoporous Tungsten Oxide Materials with High Electrical Conductivity. *Phys. Chem. Chem. Phys.* **2011**, *13*, 11060−11066.
(25) Pervez, S. A.; Kim, D.; Farooq, U.; Yaqub, A.; Choi, J.-H.; Lee, Y.-J.; Muhammad, S.; Doh, C.-H. Crystalline Iron Oxide Nanotube Arrays with High Aspect Ratio as Binder Free Anode for Li-Ion Batteries. *Phys. Status Solidi A* **2014**, *211*, 1889−1894.
(26) Reddy, M. V.; Yu, T.; Sow, C. H.; Shen, Z. X.; Lim, C. T.; Subba Rao, G. V.; Chowdari, B. V. R. α-Fe_2O_3 Nanoflakes as an Anode Material for Li-Ion Batteries. *Adv. Funct. Mater.* **2007**, *17*, 2792−2799.
(27) Zhang, J.; Yan, X.; Zhang, J.; Cai, W.; Wu, Z.; Zhang, Z. Preparation and Electrochemical Performance of TiO_2/C Composite Nanotubes as Anode Materials of Lithium-Ion Batteries. *J. Power Sources* **2012**, *198* (0), 223−228.
(28) Liu, Y.; Huang, K.; Fan, Y.; Zhang, Q.; Sun, F.; Gao, T.; Wang, Z.; Zhong, J. Binder-Free Si Nanoparticles@Carbon Nanofiber Fabric as Energy Storage Material. *Electrochim. Acta* **2013**, *102*, 246−251.
(29) Melody, B.; Kinard, T.; Lessner, P. The Non-Thickness-Limited Growth of Anodic Oxide Films on Valve Metals. *Electrochem. Solid-State Lett.* **1998**, *1* (3), 126−129.
(30) Kim, D.; Lee, K.; Roy, P.; Birajdar, B. I.; Spiecker, E.; Schmuki, P. Formation of a Non-Thickness-Limited Titanium Dioxide Mesosponge and its Use in Dye-Sensitized Solar Cells. *Angew. Chem., Int. Ed.* **2009**, *48*, 9326−9329.
(31) Lee, W.; Kim, D.; Lee, K.; Roy, P.; Schmuki, P. Direct Anodic Growth of Thick WO_3 Mesosponge Layers and Characterization of their Photoelectrochemical Response. *Electrochim. Acta* **2010**, *56*, 828−833.
(32) Kowalski, D.; Kim, D.; Schmuki, P. TiO_2 Nanotubes, Nanochannels and Mesosponge: Self-Organized Formation and Applications. *Nano Today* **2013**, *8*, 235−264.
(33) Toby, B. H. EXPGUI, A Graphical User Interface for GSAS. *J. Appl. Crystallogr.* **2001**, *34*, 210−213.
(34) Roy, P.; Berger, S.; Schmuki, P. TiO_2 Nanotubes: Synthesis and Applications. *Angew. Chem., Int. Ed.* **2011**, *50*, 2904−2939.
(35) Daniel, M. F.; Desbat, B.; Lassegues, J. C.; Garie, R. Infrared and Raman Spectroscopies of RF Sputtered Tungsten Oxide Films. *J. Solid State Chem.* **1988**, *73*, 127−139.
(36) Larcher, D.; Masquelier, C.; Bonnin, D.; Chabre, Y.; Masson, V.; Leriche, J.-B.; Tarascon, J.-M. Effect of Particle Size on Lithium Intercalation into α-Fe_2O_3. *J. Electrochem. Soc.* **2003**, *150*, A133−A139.
(37) Ryu, W.-H.; Nam, D.-H.; Ko, Y.-S.; Kim, R.-H.; Kwon, H.-S. Electrochemical Performance of a Smooth and Highly Ordered TiO_2 Nanotube Electrode for Li-Ion Batteries. *Electrochim. Acta* **2012**, *61*, 19−24.
(38) Balaya, P.; Li, H.; Kienle, L.; Maier, J. Fully Reversible Homogeneous and Heterogeneous Li Storage in RuO_2 with High Capacity. *Adv. Funct. Mater.* **2003**, *13*, 621−625.
(39) Lin, Y.-M.; Abel, P. R.; Heller, A.; Mullins, C. B. α-Fe_2O_3 Nanorods as Anode Material for Lithium Ion Batteries. *J. Phys. Chem. Lett.* **2011**, *2*, 2885−2891.

DOI: 10.1021/acsami.5b00341
ACS Appl. Mater. Interfaces 2015, 7, 7635−7643